Dalton Transactions

ROYAL SOCIETY OF CHEMISTRY

PAPER

View Article Online
View Journal | View Issue

Cite this: *Dalton Trans.*, 2025, **54**, 14199

Engineering the crystal structure and band gap of $SrTeO_4$: inducing bonding changes and metallization through compression

Ertuğrul Karaca[a,b] and Daniel Errandonea *[c]

The impact of external pressure on the characteristics of $SrTeO_4$ has been thoroughly examined using density-functional theory calculations up to 100 GPa. It has been predicted that $SrTeO_4$ undergoes three phase transitions in the pressure range covered by this study. A first transition occurs at 2.5 GPa from the ambient-pressure orthorhombic structure (space group *Pbcn*) to another orthorhombic structure described by space group *Pbcm*. A second transition occurs at 7 GPa to a monoclinic structure described by space group $P2_1/c$ and a third transition occurs at 80 GPa to another monoclinic structure described by space group $P2_1/n$. The phase transitions involve drastic changes in the atomic coordination of Sr and Te atoms. Additionally, we found that structural changes make the band-gap energy to rapidly decrease with pressure and drive metallization at 80 GPa. Moreover, we characterized the phonons and determined the compressibility of the different phases. We found that the low-pressure phase of $SrTeO_4$ exhibits a bulk modulus of 73.3(8) GPa. However, the bulk modulus is enhanced following the observed structural sequence, reaching a value of 175(6) GPa in the high-pressure phase found beyond 80 GPa. Finally, our study indicates that superconductivity is not induced by pressure in the metallic phase. Our findings provide fundamental insights into the high-pressure behavior of $SrTeO_4$.

Received 13th July 2025,
Accepted 19th August 2025

DOI: 10.1039/d5dt01643f

rsc.li/dalton

1. Introduction

Oxidotellurates(VI) of transition and alkaline-earth metals have garnered significant attention over recent decades due to their intriguing physical properties and potential applications in the energy sector.[1–7] The physical characteristics and structural integrity of compounds with compositions $ATeO_3$, A_3TeO_6, $ATeO_4$, and A_5TeO_8 (where A represents a transition or alkaline-earth metal) are known to be affected by the nature of the metal cation A. This influence is particularly evident through factors such as cationic ordering, octahedral distortion, and the arrangement of A and Te cations within the octahedral or tetrahedral sites.[1,3,8,9] This fact has motivated recent studies in $SrTeO_4$ and related compounds, which were focused on their structural, thermoelectric, and optical properties.[10] $SrTeO_4$ is a narrow-gap semiconductor and a potential thermoelectric material for mid-range temperature (600–800 K) applications, as well as PbTe, SrTe, and $PbTe_4$.[11] Compared to PbTe and SrTe, $SrTeo_4$ has the advantage that its function is not diminished by superficial oxidation products that can form under atmospheric working conditions, as it happens in PbTe and SrTe.[12] Compared to $PbTeO_4$, $SrTeO_4$ has the advantage of being a lead-free material that is less toxic and has a smaller environmental impact. As in many semiconductors, the properties of $SrTeO_4$, particularly its band gap and conductivity, can be significantly altered and tuned by applying mechanical stresses, such as compression. In some cases, the application of external pressure has driven pressure-induced metallization, a phenomenon with numerous potential applications. These include the creation of new superconducting materials, the development of high-pressure sensors, and the design of advanced materials for energy storage and conversion.

High pressure is not only a tool to tune the properties of semiconductors but it is also an effective method to better understand the properties of materials.[13] There are at least three significant applications of high-pressure techniques in both fundamental and materials science: (1) the synthesis of innovative materials that cannot be produced through other methods, (2) the phase transformation of existing materials, and (3) the exploration of fundamental systematics and rigorous testing of theoretical models. Compounds with a composition similar to that of $SrTeO_4$ have been broadly studied

[a]*Sakarya University, Faculty of Sciences, Department of Physics, 54050 Sakarya, Turkey. E-mail: ertugrulkaraca@sakarya.edu.tr*
[b]*School of Physics, Engineering & Technology, University of York, York YO10 5DD, UK. E-mail: ertugrul.karaca@york.ac.uk*
[c]*Departamento de Fisica Aplicada-ICMUV, MALTA Consolider Team, Universitat de Valencia, Av. Dr. Moliner 50, 46100 Burjassot (Valencia), Spain. E-mail: daniel.errandonea@uv.es*

under compression.[14,15] The influence of pressure on tungstates, molybdates, vanadates, phosphates, and sulphates has been deeply understood. Other compounds like selenates, chromates, antimonates, perrhenates, and arsenates have also been studied by different authors.[16–20] In contrast, $ATeO_4$ tellurates are probably among the compounds less studied under high-pressure conditions. The only tellurate studied under compression is $PbTeO_4$,[21] for which recently high-pressure has been used to synthesize a metastable polymorph in a multianvil apparatus at 8.2 GPa. This structure is monoclinic (space group $I2/a$ or alternatively $C2/c$).

$SrTeO_4$, a tellurate with technological applications as an additive in ceramics, in thermoelectric applications, and in pyrotechnics,[22] has not been studied yet under pressure. In addition, the computational modeling studies carried out previously[10] reported a crystalline structure described by space group $P2_1/c$ that is different from the structure determined by X-ray diffraction by two different groups,[23,24] which cast doubts on previous simulations. On the other hand, nothing is known about the phonons and the band structure of $SrTeO_4$ and how they are modified under compression. Given the aforementioned details, we deemed it appropriate to conduct a high-pressure study of $SrTeO_4$ at this time. We performed a density-functional theory (DFT) study exploring pressures up to 100 GPa. Utilizing DFT calculations has been proven to be an effective approach to investigate the behavior of oxides related to $SrTeO_4$ when subjected to compression.[25] We found that $SrTeO_4$ undergoes three phase transitions induced by pressure, suffers a drastic decrease in the band-gap energy, and becomes metallic at 80 GPa.

2. Methods

We carried out *ab initio* calculations employing the density-functional perturbation theory (DFPT) within the generalized-gradient approximation (GGA)[26] as implemented in the Quantum ESPRESSO simulation package.[27,28] The exchange–correlation functional was approximated using the Perdew–Burke–Ernzerhof (PBE) scheme,[26] and ultrasoft pseudopotentials were employed throughout the calculations.[29] We decided to use this approximation because it balances accuracy and computational efficiency. In addition, different authors have used it to predict high pressure phases discovered by experiments.[30] Readers should note that PBE tends to slightly underestimate the band gap energy but accurately predicts how band gaps change under pressure.[31] A plane-wave kinetic energy cut-off of 80 Ry (~1088 eV) was used for all calculations. The Kohn–Sham equations were solved with an iterative conjugate gradient scheme. The Brillouin zone (BZ) integration for total energy calculations of the low and high pressure phases of $SrTeO_4$ was carried out using the Monkhorst–Pack sampling scheme[32] with a mesh of points 16 × 16 × 16 k, corresponding to a maximum spacing of 0.01 × 2π Å^{-1}. Convergence tests are included in the SI to ensure that the results are stable and reliable. Structural optimization was carried out by minimizing the total energy and using the zero atomic force criteria. The calculations of the electronic band structure and density of states used a denser 24 × 24 × 24 k-point mesh. Phonon calculations for each structure were conducted within the harmonic approximation using the linear response method[27,28,33] in Quantum ESPRESSO, employing a 4 × 4 × 4 q-point grid for BZ sampling. The dynamical matrices were obtained on a 4 × 4 × 4 grid, and phonon properties at any q-point were obtained by Fourier interpolation.

The Migdal–Eliashberg theory[34,35] is used to calculate the electron–phonon interaction and, consequently, the superconducting critical temperature (T_c). The Eliashberg spectral function $\alpha^2F(\omega)$ is calculated by[36]

$$\alpha^2F(\omega) = \frac{1}{2\pi N(E_F)} \sum_{qj} \frac{\gamma_{qj}}{\hbar\omega_{qj}} \delta(\omega - \omega_{qj}), \quad (1)$$

where $N(E_F)$ is the electronic density of states at the Fermi energy, and α represents the average electron–phonon matrix element for phonons with energy ω in the Brillouin zone. The electron–phonon coupling (EPC) constant, $\lambda(\omega)$, can be determined by integrating the Eliashberg spectral function $\alpha^2F(\omega)$ as follows:[36,37]

$$\lambda = 2\int_0^\infty \frac{\alpha^2F(\omega)}{\omega} d\omega \quad (2)$$

The logarithmic average phonon frequency (ω_{ln}) is then calculated using

$$\omega_{ln} = \exp\left(2\lambda^{-1}\int_0^\infty \frac{d\omega}{\omega}\alpha^2F(\omega)\ln\omega\right). \quad (3)$$

Finally, the superconducting transition temperature T_c is calculated using the Allen–Dynes modification of the McMillan formula and the values of λ and ω_{ln}:

$$T_c = \frac{\omega_{ln}}{1.2}\exp\left(-\frac{1.04(1+\lambda)}{\lambda - \mu^*(1+0.62\lambda)}\right), \quad (4)$$

where μ^* is the effective screened Coulomb repulsion parameter. In most conventional superconductors, μ^* is typically in the range from 0.10 to 0.16.[36–40] In this study, we set the Coulomb pseudopotential μ^* to 0.10.

3. Results

3.1. Crystal structure and pressure-induced transitions

Strontium oxidotellurate remains largely unexamined, with previous studies focused on the orthorhombic *Pbcn* low-pressure (LP) phase.[10,23,24] In this study, we begin by optimising this phase, followed by a systematic investigation of potential high-pressure polymorphs. We examined four potential high-pressure (HP) phases of $SrTeO_4$ (HP1 (*Pbcm*, orthorhombic), HP2 ($C2/c$, monoclinic), HP3 ($P2_1/c$, monoclinic), and HP4 ($P2_1/n$, monoclinic)). These structures were chosen using the structural diagram proposed by Bastide,[41] which has been demonstrated to be an effective instrument for predicting

high-pressure crystal structures that were subsequently confirmed through experimental methods.[42,43] The HP1 phase is isostructural to $SrUO_4$,[44] HP2 is isostructural to the HP phase of $PbTeO_4$,[21] HP3 is isostructural to $CePO_4$ [45] (and it is the structure mistakenly considered in a previous DFT study[10] as the ambient-pressure structure of $SrTeO_4$), and HP4 is isostructural to $BaTeO_4$.[46] The crystal structure of the LP phase and the four potential HP phases of $SrTeO_4$ are shown in Fig. 1. The LP phase of $SrTeO_4$ is composed of linear chains of TeO_6 octahedra, which share edges and extend along the *c*-axis. The chains are held together by Sr^{2+} ions, which are coordinated by six O atoms, forming a Sr coordination octahedron with three different Sr–O bond distances and a relatively distorted structure. The calculated lattice constants for the crystal structure of the LP phase and the phases that are stable at different pressures are reported in Table 1. The calculated atomic positions for the same phases are presented in Table 2.

Fig. 2 shows the calculated enthalpy for the different phases we have considered in this work *versus* pressure. At 0 GPa the lowest enthalpy phase is the orthorhombic LP phase (space group *Pbcn*), which supports that this is the thermodynamically most stable phase of $SrTeO_4$ at ambient pressure, in agreement with X-ray diffraction experiments.[23,24] The unit-cell parameters and atomic positions determined for the LP phase (see Tables 1 and 2) are in remarkable agreement with earlier research.[23,24] The calculated lattice parameters show a

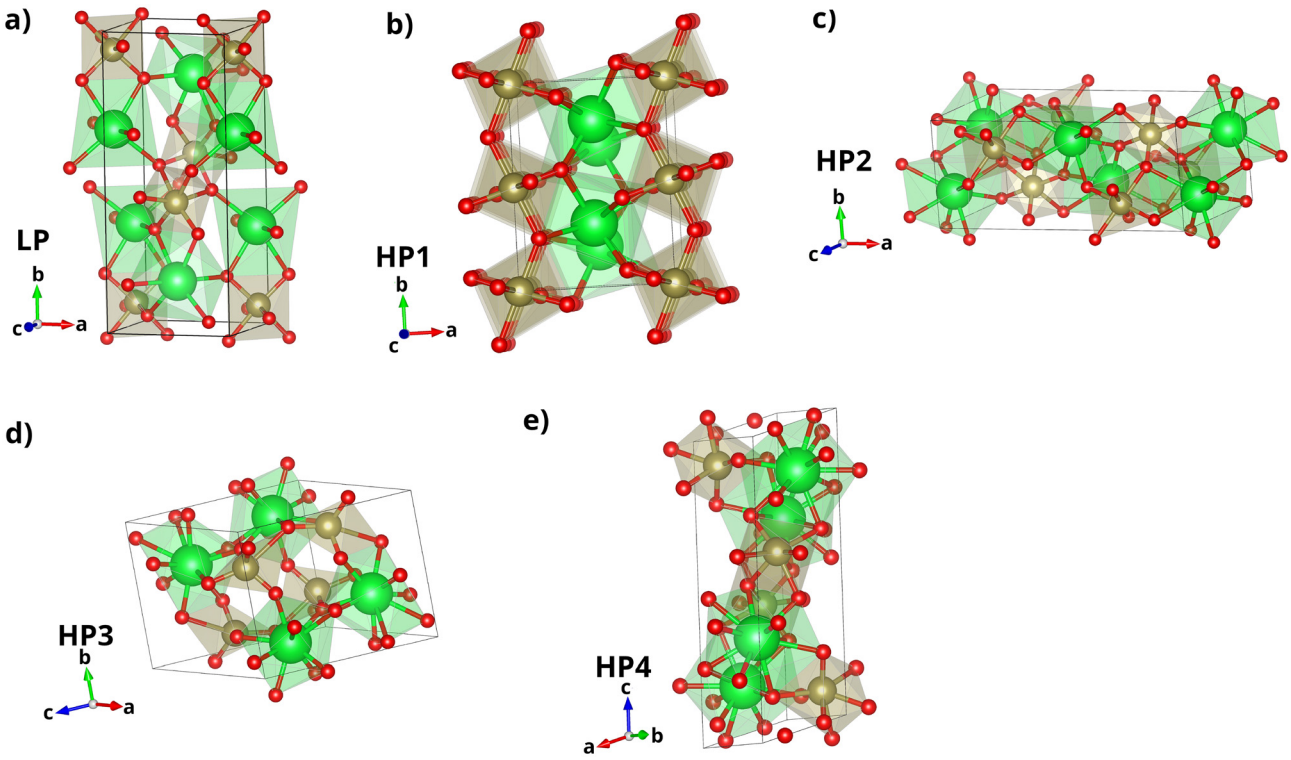

Fig. 1 The crystal structures of $SrTeO_4$ under different pressures: (a) LP (low-pressure) phase, (b) HP1 phase, (c) HP2 phase, (d) HP3 phase, and (e) HP4 phase. Green, brown, and red spheres represent Sr, Te, and O atoms, respectively. Polyhedral representations are used to highlight the coordination environments of Te (brown) and Sr (green) atoms.

Table 1 The calculated lattice parameters for the low-pressure and high-pressure phases of $SrTeO_4$ at pressures where they are stable. For the low-pressure phase, results from previous experiments[23,24] are included for comparison. The present results are shown in bold letters

Phase	*P* (GPa)	Space group	*a* (Å)	*b* (Å)	*c* (Å)	*β*°
LP (orthorhombic)	**0**	***Pbcn***	**5.664**	**13.316**	**5.134**	
Exp.[23] (orthorhombic)	0	*Pbcn*	5.574	13.114	5.001	
Exp.[24] (orthorhombic)	0	*Pbcn*	5.605	13.181	5.003	
HP1 (orthorhombic)	**0**	***Pbcm***	**5.747**	**7.589**	**7.617**	
HP1 (orthorhombic)	**5**	***Pbcm***	**5.636**	**7.488**	**7.535**	
HP3 (monoclinic)	**10**	***P*2$_1$/*c***	**5.996**	**6.293**	**7.274**	**126.6**
HP4 (monoclinic)	**80**	***P*2$_1$/*n***	**3.768**	**4.376**	**11.383**	**105.65**

Table 2 The calculated atomic positions for the LP, HP1, HP3, and HP4 structures at selected pressures (given in the table). The present results are shown in bold letters. They are compared with results from previous experiments[23,24]

	Pressure (GPa)	Atom	Site	Atomic positions		
LP	0			*x*	*y*	*z*
This work		**Sr**	**4c**	**0.0000**	**0.6665**	**0.7500**
Exp.[23]		Sr	4c	0.0000	0.6665	0.7500
Exp.[24]		Sr	4c	0.0000	0.6655	0.7500
This work		**Te**	**4c**	**0.0000**	**0.0705**	**0.7500**
Exp.[23]		Te	4c	0.0000	0.0704	0.7500
Exp.[24]		Te	4c	0.0000	0.0699	0.7500
This work		**O(1)**	**8d**	**0.3091**	**0.5425**	**0.5718**
Exp.[23]		O(1)	8d	0.3186	0.5423	0.5497
Exp.[24]		O(1)	8d	0.3145	0.5420	0.5710
This work		**O(2)**	**8d**	**0.2845**	**0.3313**	**0.6292**
Exp.[23]		O(2)	8d	0.2686	0.3284	0.6444
Exp.[24]		O(2)	8d	0.2847	0.3333	0.6322
HP1	5					
This work		**Sr**	**4d**	**0.4907**	**0.1908**	**0.2500**
This work		**Te**	**4a**	**0.0000**	**0.0000**	**0.0000**
This work		**O(1)**	**8e**	**0.6948**	**0.4258**	**0.0659**
This work		**O(2)**	**8e**	**0.1452**	**0.2500**	**0.0000**
HP3	10					
This work		**Sr**	**4e**	**0.8355**	**0.1541**	**0.7213**
This work		**Te**	**4e**	**0.3190**	**0.1777**	**0.7021**
This work		**O(1)**	**4e**	**0.3386**	**0.1281**	**0.4910**
This work		**O(2)**	**4e**	**0.6286**	**0.2278**	**0.8841**
This work		**O(3)**	**4e**	**0.0908**	**0.3554**	**0.5980**
This work		**O(4)**	**4e**	**0.1880**	**−0.0070**	**0.7610**
HP4	80					
This work		**Sr**	**4e**	**0.5001**	**0.2807**	**0.8314**
This work		**Te**	**4e**	**−0.0001**	**0.7650**	**0.4094**
This work		**O(1)**	**4e**	**0.2669**	**0.5000**	**0.7669**
This work		**O(2)**	**4e**	**0.5000**	**0.8457**	**0.8780**
This work		**O(3)**	**4e**	**0.9999**	**0.1367**	**0.4211**
This work		**O(4)**	**4e**	**0.0001**	**0.5354**	**0.2751**

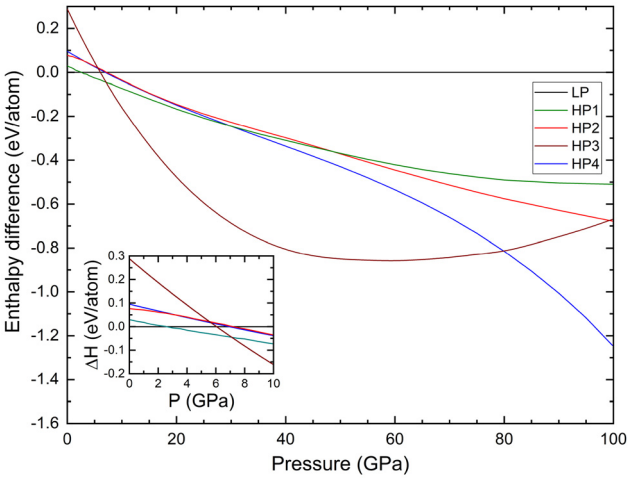

Fig. 2 The enthalpy per atom as a function of pressure for the orthorhombic low-pressure phase of $SrTeO_4$ (SG: *Pbcn*), and the high-pressure phases: HP1 (SG: *Pbcm*, orthorhombic), HP2 (SG: *C*2/*c*, monoclinic), HP3 (SG: $P2_1/c$, monoclinic), and HP4 (SG: $P2_1/n$, monoclinic). The inset show results for pressures up to 10 GPa to facilitate the identification of the transitions occurring at 2.5 and 7 GPa.

deviation of 1% from experimental results.[23,24] The results obtained for the low-pressure phase confirm the precision in the representation of the crystal structure based on the GGA-PBE approximation employed in the calculations. Our results also show that the structure proposed in a previous DFT study[10] is not the correct structure of $SrTeO_4$ having a higher enthalpy than that of the correct crystal structure of this compound (the LP phase). In addition, we noticed that the structure proposed by Abubakr *et al.*[10] has a volume which is 50% smaller than the unit-cell volume of $SrTeO_4$ and a Sr–O bond distance of 1.374 Å, a distance smaller than the covalent radii of Sr (1.95 Å), which cast serious doubts on the crystal structure proposed in the previous DFT study.[10] From our calculations, we obtained the Sr–O and Te–O bond distances for the low-pressure phase. The calculated Sr–O bond lengths are 2.528 Å (×2), 2.575 Å (×2), and 2.587 Å (×2), which agree well with experimental values.[23,24] The average Sr–O bond distance, 2.563 Å, is slightly shorter than the sum of the covalent radii of Sr (1.95 Å) and O (0.63 Å), totaling 2.58 Å. Similarly, the Te–O bond lengths are calculated to be 1.893 Å (×2), 2.009 Å (×2), and 2.067 Å (×2). In this case, the average Te–O bond distance is 1.989 Å, which is equal to the sum of the covalent radii of Te (1.36 Å) and O (0.63 Å). The calculated bond distances provide evidence for strong bonding interactions between Sr and O atoms and Te and O atoms, supporting the existence of a significant covalent character within the crystal structure.

From the results shown in Fig. 2, it can be seen that at 0 GPa the enthalpy of phase HP1 is nearly degenerated to that of the LP phase. Upon compression, phase HP1 (space group *Pbcm*) becomes the lowest enthalpy phase at 2.5 GPa, supporting the occurrence of a structural phase transition to phase HP1 at this pressure. The phase transition triggers a 13% collapse of the unit-cell volume as shown in Fig. 3. The phase transition also involves a change in the coordination of Sr atoms, involving an increase in the coordination number from 6 to 9. However, there is no change in the coordination of Te. The unit-cell parameters of phase HP1 at 0 and 5 GPa are given in Table 1. The Sr–O bond lengths in the orthorhombic HP1 phase are 2.504 Å, 2.519 Å (×2), 2.637 Å (×2), 2.745 Å (×2), and 2.785 Å (×2). The Te–O bond lengths in the orthorhombic HP1 phase are 1.874 Å (×2), 2.015 Å (×2), and 2.043 Å (×2). These results show that the TeO_6 octahedra are not very modified, and that the phase transition is related to changes in the Sr coordination environment. Phase HP1 consists of zigzag chains of corner-sharing TeO_6 octahedra, which are interconnected by SrO_9 polyhedra.

As shown in Fig. 2, our calculations predict that subsequent transitions occur at 7 GPa to phase HP3 (space group $P2_1/c$) and at 80 GPa to phase HP4 (space group $P2_1/n$). Note that phase HP3 is isomorphous to monazite. This structure was assumed to be stable at 0 GPa in previous DFT calculations.[10]

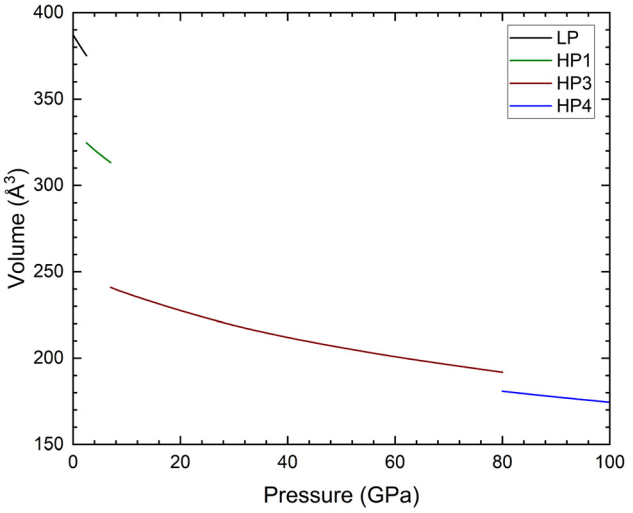

Fig. 3 Pressure dependence of the volume of the four phases of $SrTeO_4$ found from 0 to 100 GPa.

However, we have found that this structure is not the lowest enthalpy structure up to 7 GPa. In addition, the monazite-type previously reported[10] has unreasonable values of unit-cell volume and bond-distances, a fact that it is corrected in the present study. The transitions from HP1 to HP3 and from HP3 to HP4 happen with changes in the volume of 23% and 6%, respectively (see Fig. 3). Both transitions involve an important structural reorganization as shown in Fig. 1. Regarding the coordination polyhedra of Sr and Te, we found that they are modified in both transitions. The Sr and Te coordination numbers are 10 and 5 in phase HP3, and 11 and 7 in phase HP4. In both phases, the coordination polyhedra of Sr and Te are highly distorted. In HP3 at 10 GPa, Sr–O bond distances range from 2.116 Å to 2.787 Å and Te–O bond distances range from 1.538 Å to 2.371 Å. In HP4 at 80 GPa, Sr–O bond distances range from 1.971 Å to 2.525 Å and Te–O bond distances range from 1.632 Å to 1.968 Å. Our results indicate that the successive phase transition induces a considerable decrease in the Sr–O bond lengths, which will enhance orbital overlap, potentially allowing the pressure-induced transition from semiconducting to metallic behavior, a phenomenon we found to happen at 80 GPa, as we will show in the next section of the manuscript.

The existence of the predicted phase transitions could be qualitatively understood using the hypothesis proposed by Bastide, which correlates the effects of external pressure and chemical pressure.[47] According to this idea, a given oxide might take under pressure the structure of a similar oxide but with larger cations. For instance, $ZrSiO_4$ transforms under compression into the $CaWO_4$ structure.[47] This is exactly what happens in $SrTeO_4$ when external pressure is applied. It undergoes phase transitions into more compacted structures with more efficient packing with a gradual increase in the coordination number of cations. Note that the structure of phase HP4 is isomorphic to that of the densest polymorph of $BaTeO_4$,[46] having Ba ionic radii larger than those of Sr, which is consistent with the hypothesis of Bastide.

As described above, the reported phase transitions affect the coordination of both cations. In Te, the coordination number changes following the sequence 6–6–5–7 and the coordination of Sr changes following the sequence 6–9–10–11. Under high pressure, cation coordination in oxides generally shifts towards higher coordination numbers, leading to more compact and denser structures. This is because the increased pressure forces the atoms closer together, favoring configurations where cations are surrounded by more anions. Therefore, the changes found in the Sr and Te environment are chemically plausible. In $SrTeO_4$, the coordination environment of Sr is more affected than that of Te. This is related to two facts. The first one is their contrasting ionic radii and charge. Sr, being a larger ion with a +2 charge, tends to adopt under compression a higher coordination number with oxygen atoms, while Te, with a +6 charge and smaller ionic radius, maintains a coordination close to octahedral. The second one is that the ionic interaction Sr–O is more easily open to coordination changes than the (at least partially) covalent Te–O interaction.

The successive phase transitions also affect the compressibility of $SrTeO_4$ as shown in Fig. 3. We have fitted our results with the third-order Birch–Murnaghan equation of state[48] and determined the volume at zero pressure (V_0), the bulk modulus (B_0), and its pressure derivative (B_0'). The parameters obtained are summarized in Table 3. The bulk modulus of the low-pressure phase of $SrTeO_4$, 75 GPa, is similar to the same parameter in related ternary strontium oxides. In $SrSeO_4$ B_0 = 58 GPa,[49] in $SrSO_4$ B_0 = 62 GPa,[50] in $SrCrO_4$ B_0 = 59 GPa,[51] in $SrUO_4$ B_0 = 66 GPa,[52] in $SrWO_4$ B_0 = 66 GPa,[53] and in $SrMoO_4$ B_0 = 71 GPa.[54] This is not surprising since, as a first approximation in ternary oxides, the change in volume under compression is mainly caused by the contraction of the coordination polyhedra or the largest cation.[55] In all of the compounds mentioned above, this is the Sr coordination polyhedra. More recently, Errandonea and Manjon[47] applied this idea to ternary oxides. Applying the empirical formula derived by these authors to $SrTeO_4$, a bulk modulus of 72 GPa is obtained, which is fully consistent with the present results and supports the hypothesis that the volume change in the LP phase of $SrTeO_4$ is mainly caused by the contraction of Sr–O

Table 3 The calculated equilibrium volume V_0 (Å^3) at 0 GPa, bulk modulus K_0 (in GPa) at 0 GPa, and its pressure derivative K_0' for the LP, HP1, HP3, and HP4 phases

Phase	V_0	K_0	K_0'
LP	**387.22(3)**	**73.3(8)**	**4.1(6)**
HP1	**332.1(1)**	**103(2)**	**4.8(5)**
HP3	**251.1(6)**	**153(4)**	**4.9(5)**
HP4	**231.1(9)**	**175(6)**	**4.9(5)**

bonds. With regard to the increase of the bulk modulus at the successive phase transitions, this phenomenon is consistent with the discontinuous decrease of the volume at each transition, which triggers an increase of the density of the material. This increase is often accompanied by an increase in compression resistance, which is reflected in the increase in the bulk modulus.[56]

3.2. Electronic properties of $SrTeO_4$

In addition to the structural behavior of $SrTeO_4$, we examined the electronic properties of this material by calculating the band structures and the corresponding total and partial electronic densities of states (DOS and PDOS) for the low-pressure and high-pressure phases. The results are shown in Fig. 4. The LP phase of $SrTeO_4$ exhibits an indirect band gap of 2.03 eV. To the best of our knowledge, there are no experimental results to compare with. We will then compare with studies on $CoTeO_4$,[57] $SrSeO_4$, and $SrCrO_4$.[49] $CoTeO_4$ has a band-gap energy of 2.42 eV according to optical-absorption spectroscopy.[57] It is therefore reasonable that for the related tellurate $SrTeO_4$ we obtained a slightly smaller band-gap energy, 2.04 eV, considering that DFT calculations within the PBE scheme tend to slightly underestimate the band-gap energy.[58] On the other hand, the band gaps of $SrSeO_4$ and $SrCrO_4$,[49] obtained from similar DFT calculations, are 3.61 and 2.67 eV, respectively. This aligns with the observation that the band-gap energy of selenates is typically greater than that of chromates, which in turn is generally greater than that of tellurates. In the LP phase of $SrTeO_4$ the valence band maximum (VBM) is located at the Y point in the BZ. The conduction band minimum (CBM) occurs at the Γ point in the BZ, as shown in Fig. 4(a). The energy difference between the valence-band edges at the Y and Γ points is only 0.02 eV, suggesting that $SrTeO_4$ is close to a direct-gap regime. This near-degeneracy of the valence band edges can improve optical transitions by enabling thermal and external effects to overcome the small splitting, thereby allowing tunable optical behavior in pressure-sensitive optoelectronic devices.

For a more comprehensive analysis of the electronic band structure, we calculated the density of states (DOS), as shown in Fig. 4. The bands between −20.4 eV and −15.7 eV in the LP phase of $SrTeO_4$ are dominated by the s-states of O atoms, while the contributions from other atoms in this energy range are negligible, which is expected for low-energy s-states. Around −14 eV, a sharp and high-intensity peak appears in the DOS, mostly coming from the Sr 4p states. This sharp characteristic reflects the localized nature of the Sr 4p orbitals, with negligible contributions from O or Te atoms in this energy range. In the energy range between −11.0 and −7.5 eV, the DOS reveals nearly equal and overlapping contributions from Te 5s and O 2s and 2p orbitals. In addition, hybridization between Te 5p and O 2s orbitals is observed in this energy range, confirming the existence of a strong covalent interaction between Te and O atoms. In the valence band region between −6.5 eV and −3.1 eV, the electronic states are primarily dominated by O 2p orbitals. In the energy range of −3.1 eV to the Fermi level, the valence band is mostly formed of O 2p orbitals, showing that oxygen plays a major role at the top of the valence band. The bands in the energy range between 2.03 and 4 eV primarily originate from the hybridization between Te 5s and O 2p orbitals, indicating a mixed character at the bottom of the conduction band. This significant hybridization leads to a dispersive conduction band with a low effective electron mass, which is advantageous for high carrier mobility and suggests promising optoelectronic device performance. Additionally, the mixed orbital character may enhance optical transition strengths and enable tunability of electronic properties under external factors such as pressure or strain.

We also analyzed the electronic properties of $SrTeO_4$ by comparing the LP (orthorhombic *Pbcn*) and the HP1 phases (orthorhombic *Pbcm*), both calculated at 0 GPa to enable a direct comparison. The electronic band structures and DOS characteristics of both phases are broadly similar, indicating that the main orbital interactions are not significantly affected by the structural differences. The energy levels, peak positions and orbital contributions, including Te–O hybridization, are close to the same, indicating that the covalent bonding character is mainly unchanged across the transition. As shown in Fig. 4, the band gap decreases from 2.03 eV in the LP phase to 1.40 eV in the HP1 phase at ambient pressure. In addition, the DOS patterns between −20.4 eV and −15.7 eV reveal four peaks for the LP phase, while only three peaks are present in the HP1 phase, and all peaks show a reduced intensity compared to those in the LP phase. The fewer and weaker peaks suggest that the electronic states have been slightly modified by the structural change.

We next examined the electronic properties of the HP3 phase, which is stable from 7 to 80 GPa. The band structure and PDOS at 7 GPa (see Fig. 4) show that the general characteristics of orbital hybridization and atomic contributions to the valence and conduction bands remain very similar to those observed in the LP and HP1 phases. However, the intensity of all peaks is significantly reduced, especially the peak at about 14 eV related to Sr 4p states. In addition, the lowest valence bands shift from −20 eV in the LP and HP1 phases to −24 eV in the HP3 phase, indicating stronger binding and increased structural stability under pressure. The HP4 phase of $SrTeO_4$, stable at 80 GPa, exhibits metallic behavior at this pressure, as confirmed by both the band structure and density of states (DOS) analyses (see Fig. 4). The atomic contributions to the electronic band structures of the HP3 and HP4 phases are notably similar. The lowest-energy valence bands in HP3 are separated by a minor gap of about 0.1 eV; however, this gap vanishes in the HP4 phase at 80 GPa. A similar behavior is observed at around −14 eV for the Sr 4p-derived bands: in HP3, there is a gap of about 0.5 eV between these bands and the higher-energy valence bands; however, this separation disappears in HP4. Finally, the energy gap between the valence and conduction bands vanishes in HP4, confirming its metallic nature at 80 GPa. In the HP4 phase, the total density of states (DOS) at the Fermi level has been calculated to be 3.069 states per eV, mainly coming from O 2p orbitals (2.450 states per eV, 79%) and Te 5s orbitals (0.520 states per eV, about

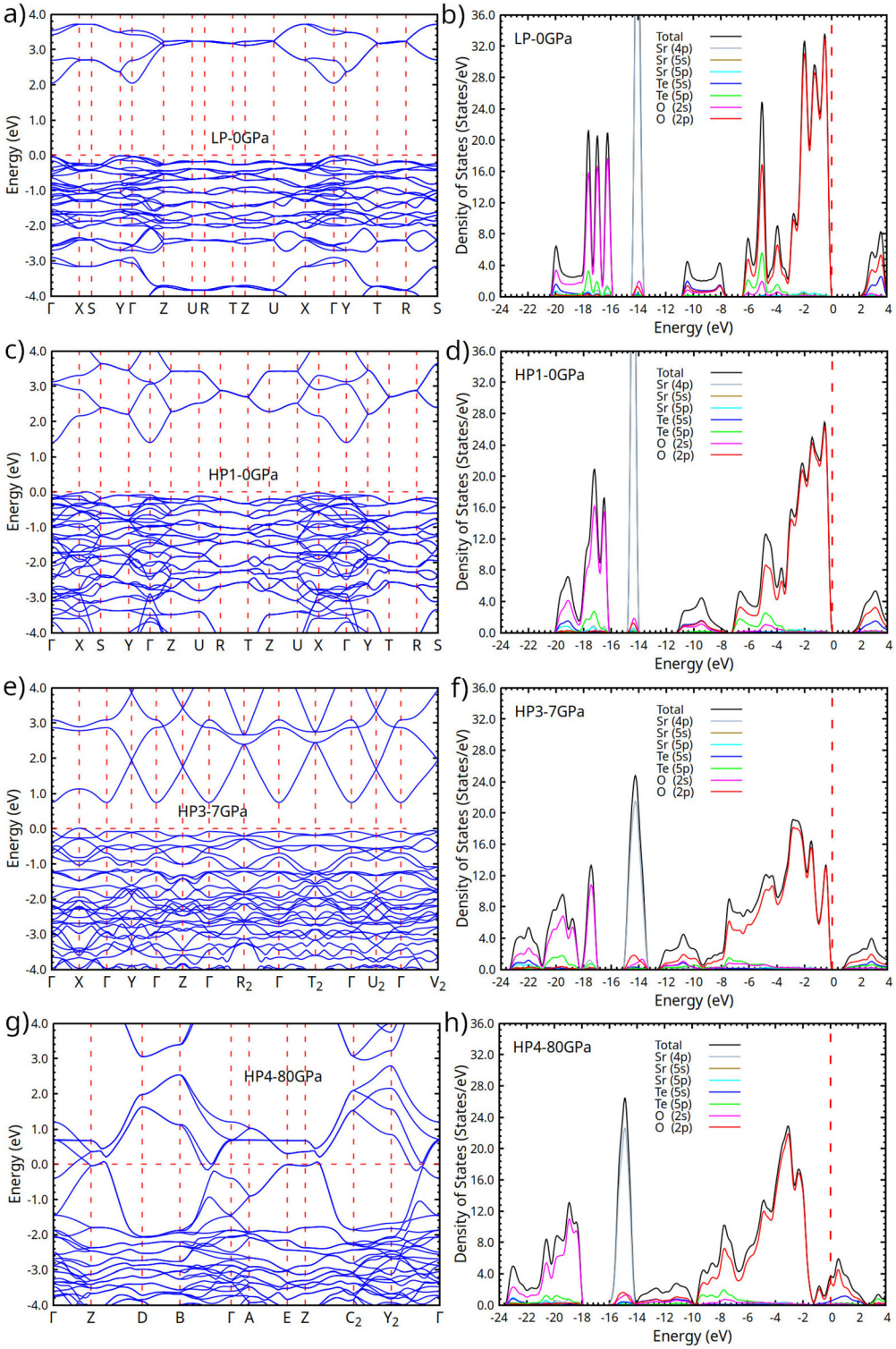

Fig. 4 The electronic band structures (left panels) and total and partial densities of states (right panels) of $SrTeO_4$ for (a, b) the LP phase at 0 GPa, (c, d) the HP1 phase at 0 GPa, (e, f) the HP3 phase at 7 GPa, and (g, h) the HP4 phase at 80 GPa. The Fermi level is set to 0 eV.

17%). This suggests that the electrical conductivity for HP4 particularly originates from oxygen and tellurium atoms. This behavior indicates a pressure-induced insulator-to-metal transition, which is mainly caused by increased Te–O orbital hybridization. The contribution of Sr atoms to $N(E_F)$ is negligible, indicating that Sr behaves fully as Sr^{2+} in the HP4 phase.

We then examined the pressure-dependence of the band gap (E_g) and electronic density of states (DOS) at the Fermi

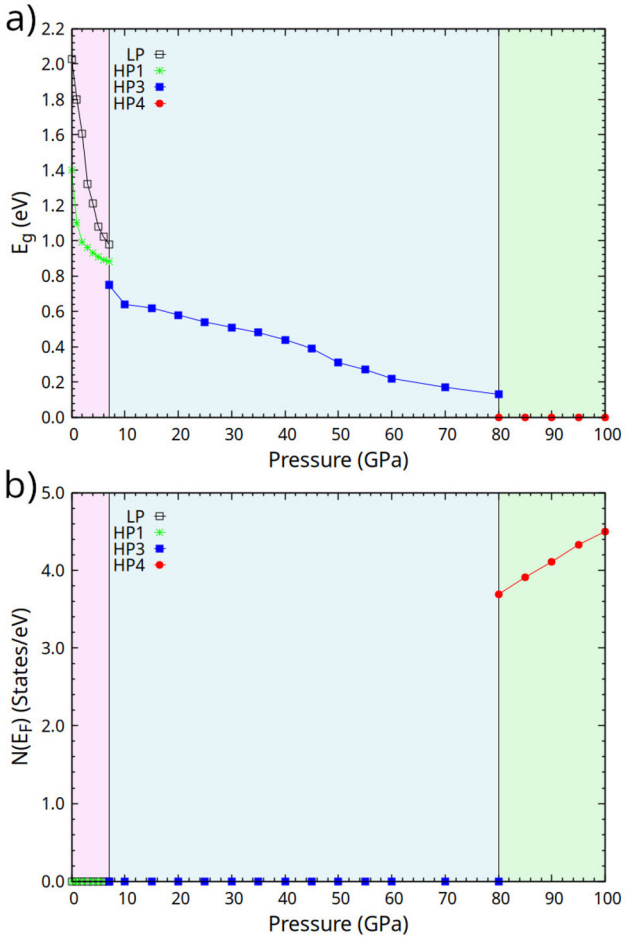

Fig. 5 (a) Pressure dependence of the electronic band gap (E_g) and (b) the electronic density of states at the Fermi level ($N(E_F)$) for $SrTeO_4$ in different structural phases. LP (□, black), HP1 (*, green), HP3 (■, blue), and HP4 (●, red) phases are represented by different symbols and colors.

level ($N(E_F)$). The results are given in Fig. 5, where panel (a) shows the pressure dependence of the band gap (E_g), and panel (b) presents the corresponding $N(E_F)$ for both the LP and the four high-pressure phases of $SrTeO_4$. Fig. 5(a) shows that the LP phase and the HP1 phase, stable at 2.5 GPa, both have semiconducting properties, with band gaps that gradually decrease as pressure increases. The band gap of the HP3 phase, which is stable from 7 to 80 GPa, is calculated to be 0.75 eV at 7 GPa, which is lower than that of the LP (0.980 eV) and HP1 (0.883 eV) phases at the same pressure, and continues to decrease with increasing pressure until the phase transition at 80 GPa. The HP3 phase remains semiconducting up to 80 GPa, despite the decreasing band gap. The band-gap energy of phase HP3 at 80 HPa is 0.15 GPa. The HP4 phase becomes thermodynamically stable at 80 GPa and exhibits a metallic character at that pressure. As shown in Fig. 5(b), the density of states at the Fermi level, $N(E_F)$, increases significantly to 3.609 states per eV at 80 GPa, indicating the beginning of metallic behavior. Upon further compression, $N(E_F)$ increases linearly, reaching 4.501 states per eV at 100 GPa. The results show that pressure significantly influences the electronic structure of $SrTeO_4$, leading to an insulator-to-metal transition and increased conductivity in the high-pressure phase.

3.3. Phonon properties of $SrTeO_4$

Phonon calculations are crucial for determining the dynamical stability of $SrTeO_4$ under pressure and for understanding its vibrational properties and structural transitions. Therefore, we performed phonon calculations for the LP and HP1 phases at 0 GPa to allow a direct comparison under similar conditions, comparable to the electronic structure analysis. Furthermore, the phonon spectra of HP3 at 7 GPa and HP4 at 80 GPa have been determined, corresponding to the pressures at which these phases become thermodynamically stable. All $SrTeO_4$ structures analyzed in this study consist of four formula units per unit cell, totaling 24 atoms. As a result, the phonon dispersion curve contains 72 vibrational modes, which include 3 acoustic and 69 optical phonon modes.

The zone-center optical phonon modes of the LP phase can be classified according to the irreducible representations of the point group D_{2h}. The symmetry of these optical phonon modes is predicted by group theory in the following form: $\Gamma = 8(A_g + A_u) + 10(B_{1g} + B_{2g}) + 8B_{3g} + 9(B_{1u} + B_{2u}) + 7B_{3u}$, where the B_{1u}, B_{2u}, and B_{3u} modes are infrared-active (IR), while the A_g, B_{1g}, B_{2g}, and B_{3g} modes are Raman-active (R). The A_u modes are silent. The calculated zone-center phonon frequencies at the Γ point for the LP phase of $SrTeO_4$ at 0 GPa are given in Table 4, together with their mode symmetries and the atomic contributions to each vibration. The corresponding results for the HP1, HP3, and HP4 phases are presented in Tables 5, 6, and 7 respectively. To our knowledge, no IR or Raman experiments have been previously reported for any of the phases of $SrTeO_4$. However, a Raman study was carried out for $CoTeO_4$.[7] Interestingly, both compounds have four Raman-active high-frequency modes separated by more than 100 cm^{-1} from the rest of the modes. These are internal stretching modes of the coordination polyhedron of Te. These phonons are at 780, 704, 643, and 626 cm^{-1} in $CoTeO_4$ and at 737, 681, 630, and 610 cm^{-1} in $SrTeO_4$. The similarities between the frequencies of the internal stretching modes of the Te coordination polyhedron in both compounds make us confident about the accuracy of our calculations.

Our results also support that the optical phonon modes in the LP phase are mainly determined by vibrations of Te and O atoms, thereby confirming the strong covalent character of Te–O bonding in $SrTeO_4$. The wide frequency range of Raman-active (49–737 cm^{-1}) and infrared-active (50–707 cm^{-1}) phonon modes in $SrTeO_4$ highlights the vibrational complexity of the crystal and suggests that Te–O bonds are crucial in both polarizability and dipole-related lattice dynamics. The eigenvector analysis of zone-center optical phonon modes in the LP phase of $SrTeO_4$ shows different atomic contributions in the vibrational spectrum. The low-frequency modes (<150 cm^{-1}) mainly contain Sr atom motions, consistent with its large

Table 4 The calculated zone-center optical phonon frequencies (ν in cm^{-1}) and dominant atomic contributions (eigen characteristics) for the LP phase of $SrTeO_4$ (orthorhombic *Pbcn*) at 0 GPa. IR, R, and S denote infrared-active, Raman-active, and silent modes, respectively. The atom contributing most significantly to each mode is shown in bold. Mode symmetries are also indicated

Mode	(ν) (cm^{-1})	Eigen characters	Mode	(ν) (cm^{-1})	Eigen characters
A_g (R)	**119.42**	**Sr** + Te + O	**B_{2g} (R)**	**61.66**	Sr + Te + **O**
A_g (R)	**178.27**	Te + **O**	**B_{2g} (R)**	**94.72**	**Sr**
A_g (R)	**222.07**	Sr + **O**	**B_{2g} (R)**	**141.47**	**Sr** + Te + O
A_g (R)	**287.31**	**O**	**B_{2g} (R)**	**179.39**	**Te** + O
A_g (R)	**389.45**	**O**	**B_{2g} (R)**	**232.22**	Te + **O**
A_g (R)	**491.27**	**O**	**B_{2g} (R)**	**266.07**	Te + **O**
A_g (R)	**608.35**	**O**	**B_{2g} (R)**	**344.95**	Te + **O**
A_g (R)	**734.32**	**O**	**B_{2g} (R)**	**502.91**	**O**
B_{1g} (R)	**49.02**	**Sr** + Te + O	**B_{2g} (R)**	**630.95**	**O**
B_{1g} (R)	**110.05**	**Sr** + Te + O	**B_{2g} (R)**	**671.49**	**O**
B_{1g} (R)	**127.28**	**Sr** + O	**B_{3g} (R)**	**145.81**	**Sr** + O
B_{1g} (R)	**180.47**	Sr + **Te** + O	**B_{3g} (R)**	**199.38**	**O**
B_{1g} (R)	**227.29**	**O**	**B_{3g} (R)**	**220.37**	Sr + **Te** + O
B_{1g} (R)	**267.15**	Te + **O**	**B_{3g} (R)**	**293.63**	**O**
B_{1g} (R)	**342.07**	Te + **O**	**B_{3g} (R)**	**418.24**	**O**
B_{1g} (R)	**506.49**	**O**	**B_{3g} (R)**	**499.24**	**O**
B_{1g} (R)	**630.53**	**O**	**B_{3g} (R)**	**609.87**	**O**
B_{1g} (R)	**681.49**	**O**	**B_{3g} (R)**	**737.89**	**O**
B_{1u} (IR)	**50.41**	Sr + Te + **O**	**B_{2u} (IR)**	**239.00**	**O**
B_{1u} (IR)	**91.98**	**Sr** + Te + O	**B_{2u} (IR)**	**321.31**	Te + **O**
B_{1u} (IR)	**127.32**	**Sr** + O	**B_{2u} (IR)**	**471.61**	**O**
B_{1u} (IR)	**212.48**	**O**	**B_{2u} (IR)**	**543.34**	Te + **O**
B_{1u} (IR)	**235.45**	Te + **O**	**B_{2u} (IR)**	**669.48**	Te + **O**
B_{1u} (IR)	**322.79**	Te + **O**	**B_{3u} (IR)**	**155.66**	**Sr** + Te + O
B_{1u} (IR)	**470.31**	**O**	**B_{3u} (IR)**	**207.89**	**O**
B_{1u} (IR)	**544.52**	Te + **O**	**B_{3u} (IR)**	**345.94**	**O**
B_{1u} (IR)	**680.42**	Te + **O**	**B_{3u} (IR)**	**402.71**	**O**
B_{2u} (IR)	**52.83**	Sr + Te + **O**	**B_{3u} (IR)**	**515.06**	**O**
B_{2u} (IR)	**106.02**	Sr + Te + **O**	**B_{3u} (IR)**	**582.91**	**O**
B_{2u} (IR)	**121.34**	Sr + Te + **O**	**B_{3u} (IR)**	**706.82**	**O**
B_{2u} (IR)	**217.26**	**O**			
A_u (S)	**101.80**	Sr + **Te** + O	**A_u (S)**	**399.88**	**O**
A_u (S)	**137.70**	**Sr** + O	**A_u (S)**	**538.16**	**O**
A_u (S)	**184.49**	**O**	**A_u (S)**	**609.18**	**O**
A_u (S)	**355.75**	**O**	**A_u (S)**	**739.03**	**O**

Table 5 The calculated zone-center optical phonon frequencies (ν in cm^{-1}) and dominant atomic contributions (eigen characteristics) for the HP1 phase of $SrTeO_4$ (orthorhombic *Pbcm*) at 0 GPa. IR, R, and S denote infrared-active, Raman-active, and silent modes, respectively. The atom contributing most significantly to each mode is shown in bold. Mode symmetries are also indicated

Mode	(ν) (cm^{-1})	Eigen characters	Mode	(ν) (cm^{-1})	Eigen characters
A_g (R)	**90.21**	**Sr** + O	**B_{1g} (R)**	**596.00**	**O**
A_g (R)	**117.59**	**Sr** + O	**B_{1g} (R)**	**697.48**	**O**
A_g (R)	**225.57**	**O**	**B_{2g} (R)**	**145.64**	**Sr** + O
A_g (R)	**272.24**	**O**	**B_{2g} (R)**	**237.97**	**O**
A_g (R)	**290.52**	**O**	**B_{2g} (R)**	**270.54**	**O**
A_g (R)	**441.67**	**O**	**B_{2g} (R)**	**436.68**	**O**
A_g (R)	**460.67**	**O**	**B_{2g} (R)**	**627.06**	**O**
A_g (R)	**715.98**	**O**	**B_{2g} (R)**	**707.84**	**O**
B_{1g} (R)	**56.18**	**O**	**B_{3g} (R)**	**73.67**	**Sr** + O
B_{1g} (R)	**120.11**	**Sr** + O	**B_{3g} (R)**	**210.43**	**O**
B_{1g} (R)	**160.41**	**Sr** + O	**B_{3g} (R)**	**246.81**	**O**
B_{1g} (R)	**248.57**	**O**	**B_{3g} (R)**	**284.42**	**O**
B_{1g} (R)	**280.08**	**O**	**B_{3g} (R)**	**531.17**	**O**
B_{1g} (R)	**359.77**	**O**	**B_{3g} (R)**	**616.90**	**O**
B_{1g} (R)	**460.89**	**O**	**B_{3g} (R)**	**696.30**	**O**
B_{1u} (IR)	**94.46**	**Sr** + Te + O	**B_{2u} (IR)**	**390.53**	Te + **O**
B_{1u} (IR)	**100.25**	**Sr** + Te + O	**B_{2u} (IR)**	**442.77**	Te + **O**
B_{1u} (IR)	**153.86**	Te + **O**	**B_{2u} (IR)**	**475.51**	Te + **O**
B_{1u} (IR)	**206.66**	Te + **O**	**B_{2u} (IR)**	**725.30**	Te + **O**
B_{1u} (IR)	**214.17**	Te + **O**	**B_{3u} (IR)**	**80.09**	**Sr** + Te + O
B_{1u} (IR)	**262.79**	Te + **O**	**B_{3u} (IR)**	**111.28**	**Sr** + Te + O
B_{1u} (IR)	**531.18**	**O**	**B_{3u} (IR)**	**156.64**	Te + **O**
B_{1u} (IR)	**581.41**	Te + **O**	**B_{3u} (IR)**	**205.83**	Te + **O**
B_{1u} (IR)	**702.75**	Te + **O**	**B_{3u} (IR)**	**214.85**	Te + **O**
B_{2u} (IR)	**134.77**	**Sr** + Te + O	**B_{3u} (IR)**	**229.89**	Te + **O**
B_{2u} (IR)	**153.16**	**Sr** + Te + O	**B_{3u} (IR)**	**286.43**	Te + **O**
B_{2u} (IR)	**199.74**	**Te** + O	**B_{3u} (IR)**	**414.00**	Te + **O**
B_{2u} (IR)	**250.91**	Te + **O**	**B_{3u} (IR)**	**451.13**	Te + **O**
B_{2u} (IR)	**264.48**	Te + **O**	**B_{3u} (IR)**	**542.02**	**O**
B_{2u} (IR)	**363.60**	Te + **O**	**B_{3u} (IR)**	**723.07**	Te + **O**
A_u (S)	**95.02**	Te + **O**	**A_u (S)**	**363.10**	Te + **O**
A_u (S)	**116.06**	**Sr** + Te + O	**A_u (S)**	**422.29**	Te + **O**
A_u (S)	**135.66**	Te + **O**	**A_u (S)**	**582.84**	**O**
A_u (S)	**209.34**	Te + **O**	**A_u (S)**	**712.65**	**O**
A_u (S)	**238.61**	Te + **O**			

atomic mass. In the mid-frequency range (150–400 cm^{-1}), both Te and O atoms make a significant contribution, and their vibrational interaction is observed in a high-frequency range. The existence of Te-related modes at high frequencies, despite the fact that Te is heavier than Sr, suggests that the Te–O bonds in $SrTeO_4$ are stronger than the Sr–O bonds. At higher frequencies (>500 cm^{-1}), oxygen atoms dominate the vibrations. Similar behaviors are seen in both the infrared-active and silent modes, highlighting the importance of Te–O bonding in determining the vibrational behavior of $SrTeO_4$.

The HP1 phase (*Pbcm*) zone-center optical phonon modes are given the same point group D_{2h} as the LP phase; however, their distribution of zone-center optical phonon modes is different. Specifically, the LP phase exhibits $8A_g$, $10B_{1g}$, $10B_{2g}$, $8B_{3g}$, $9B_{1u}$, $9B_{2u}$, $7B_{3u}$, and 8 A_u modes, whereas the HP1 phase contains $8A_g$, $9B_{1g}$, $6B_{2g}$, $7B_{3g}$, $9B_{1u}$, $10B_{2u}$, $11B_{3u}$, and 9 A_u modes. The eigenvector analysis shows that, as in the LP phase, in the HP1 phase, the low-frequency Raman-active modes involve Sr atom vibrations, while mid- and high-frequency modes are dominated by oxygen contributions, with a significant Te–O hybridization. The high frequency modes in HP1, which extend up to 715–725 cm^{-1}, are mainly dominated by oxygen and are related to the internal stretching vibrations of the Te coordination polyhedron. Our results confirm the persistence of strong Te–O covalent bonding under pressure.

The HP3 phase of $SrTeO_4$, stabilized at 7 GPa, belongs to the point group C_{2h}, which results in a different symmetry classification compared to the LP and HP1 phases. An analysis using group theory yields the following distribution of zone-center phonon modes: $\Gamma = 18A_g + 18B_g + 17A_u + 16B_u$, where the A_g and B_g modes are Raman-active, and the A_u and B_u modes are infrared-active. The calculated phonon modes and eigenvector analysis (Table 6) show that the vibrational behavior in HP3 is notably richer and more delocalized compared to

Table 6 The calculated zone-center optical phonon frequencies (ν in cm^{-1}) and dominant atomic contributions (eigen characteristics) for the HP3 phase of $SrTeO_4$ (monoclinic $P2_1/c$) at 7 GPa. IR and R denote infrared-active and Raman-active modes, respectively. The atom contributing most significantly to each mode is shown in bold. Mode symmetries are also indicated

Mode	(ν) (cm^{-1})	Eigen characters	Mode	(ν) (cm^{-1})	Eigen characters
A_g (R)	**64.15**	**Sr** + Te + O	**B_g (R)**	**52.51**	**Sr** + Te + O
A_g (R)	**80.74**	Sr + **Te** + O	**B_g (R)**	**68.38**	Sr + Te + **O**
A_g (R)	**95.93**	Sr + Te + **O**	**B_g (R)**	**98.29**	Sr + Te + **O**
A_g (R)	**121.77**	Sr + **Te** + O	**B_g (R)**	**112.29**	Sr + Te + **O**
A_g (R)	**131.84**	Sr + **Te** + O	**B_g (R)**	**139.44**	Sr + Te + **O**
A_g (R)	**156.05**	Sr + Te + **O**	**B_g (R)**	**159.82**	Sr + Te + **O**
A_g (R)	**162.64**	Sr + Te + **O**	**B_g (R)**	**183.43**	Sr + Te + **O**
A_g (R)	**225.53**	Sr + Te + **O**	**B_g (R)**	**205.81**	Sr + Te + **O**
A_g (R)	**247.29**	Te + **O**	**B_g (R)**	**235.67**	Sr + Te + **O**
A_g (R)	**260.71**	Te + **O**	**B_g (R)**	**269.11**	Te + **O**
A_g (R)	**325.84**	**Te** + O	**B_g (R)**	**341.42**	**Te** + O
A_g (R)	**337.22**	Te + **O**	**B_g (R)**	**353.68**	**O**
A_g (R)	**359.17**	Te + **O**	**B_g (R)**	**386.70**	Te + **O**
A_g (R)	**395.20**	**O**	**B_g (R)**	**414.39**	Te + **O**
A_g (R)	**678.01**	**Te** + O	**B_g (R)**	**691.43**	Te + **O**
A_g (R)	**691.95**	Te + **O**	**B_g (R)**	**705.64**	**Te** + O
A_g (R)	**704.21**	**O**	**B_g (R)**	**718.69**	Te + **O**
A_g (R)	**716.09**	**O**	**B_g (R)**	**731.53**	**O**
A_u (IR)	**71.07**	**Sr** + Te + O	**B_u (IR)**	**68.94**	Sr + Te + **O**
A_u (IR)	**94.46**	Te + **O**	**B_u (IR)**	**106.82**	Sr + Te + **O**
A_u (IR)	**116.13**	Sr + Te + **O**	**B_u (IR)**	**138.37**	Sr + Te + **O**
A_u (IR)	**135.74**	**Sr** + Te + O	**B_u (IR)**	**156.58**	**Sr** + Te + O
A_u (IR)	**167.15**	Sr + Te + **O**	**B_u (IR)**	**171.36**	Sr + Te + **O**
A_u (IR)	**189.04**	Sr + Te + **O**	**B_u (IR)**	**211.33**	Sr + Te + **O**
A_u (IR)	**203.67**	Sr + **Te** + O	**B_u (IR)**	**219.49**	Te + **O**
A_u (IR)	**219.52**	Sr + **Te** + O	**B_u (IR)**	**268.74**	**Te** + O
A_u (IR)	**239.64**	Sr + **Te** + O	**B_u (IR)**	**328.44**	Te + **O**
A_u (IR)	**296.06**	**Te** + O	**B_u (IR)**	**359.62**	Te + **O**
A_u (IR)	**352.21**	Te + **O**	**B_u (IR)**	**370.46**	Te + **O**
A_u (IR)	**387.00**	Te + **O**	**B_u (IR)**	**382.94**	Te + **O**
A_u (IR)	**419.94**	Te + **O**	**B_u (IR)**	**668.46**	**Te** + O
A_u (IR)	**680.11**	Te + **O**	**B_u (IR)**	**691.01**	Te + **O**
A_u (IR)	**692.91**	**O**	**B_u (IR)**	**696.27**	**O**
A_u (IR)	**695.34**	**Te** + O	**B_u (IR)**	**726.10**	**O**
A_u (IR)	**727.03**	Te + **O**			

Table 7 The calculated zone-center optical phonon frequencies (ν in cm^{-1}) and dominant atomic contributions (eigen characteristics) for the HP4 phase of $SrTeO_4$ (monoclinic $P2_1/n$) at 80 GPa. IR and R denote infrared-active and Raman-active modes, respectively. The atom contributing most significantly to each mode is shown in bold. Mode symmetries are also indicated

Mode	(ν) (cm^{-1})	Eigen characters	Mode	(ν) (cm^{-1})	Eigen characters
A_g (R)	**53.450**	**Sr** + Te + O	**B_g (R)**	**65.229**	Sr + Te + **O**
A_g (R)	**100.634**	**Sr** + Te + O	**B_g (R)**	**83.353**	**Sr** + Te + O
A_g (R)	**114.178**	**Sr** + Te + O	**B_g (R)**	**129.404**	**Sr** + Te + O
A_g (R)	**122.370**	**Sr** + Te + O	**B_g (R)**	**137.849**	**Sr** + Te + O
A_g (R)	**177.775**	Sr + Te + **O**	**B_g (R)**	**186.226**	Te + **O**
A_g (R)	**189.514**	**O**	**B_g (R)**	**207.780**	Te + **O**
A_g (R)	**211.813**	Sr + Te + **O**	**B_g (R)**	**215.441**	Te + **O**
A_g (R)	**220.725**	Te + **O**	**B_g (R)**	**225.381**	Te + **O**
A_g (R)	**266.304**	Te + **O**	**B_g (R)**	**268.001**	Te + **O**
A_g (R)	**283.937**	Te + **O**	**B_g (R)**	**292.210**	**O**
A_g (R)	**337.772**	Te + **O**	**B_g (R)**	**340.790**	Te + **O**
A_g (R)	**366.277**	**O**	**B_g (R)**	**391.951**	**O**
A_g (R)	**458.319**	**O**	**B_g (R)**	**466.201**	**O**
A_g (R)	**475.779**	**O**	**B_g (R)**	**474.467**	**O**
A_g (R)	**552.787**	**O**	**B_g (R)**	**555.068**	**O**
A_g (R)	**580.026**	Te + **O**	**B_g (R)**	**579.023**	**O**
A_g (R)	**593.348**	**O**	**B_g (R)**	**584.619**	Te + **O**
A_g (R)	**667.687**	**O**	**B_g (R)**	**668.122**	**O**
A_u (IR)	**50.069**	Sr + Te + **O**	**B_u (IR)**	**53.200**	Sr + **Te** + O
A_u (IR)	**79.381**	**Sr** + Te + O	**B_u (IR)**	**89.211**	**Sr** + Te + O
A_u (IR)	**94.014**	Sr + **Te** + O	**B_u (IR)**	**115.943**	**Sr** + Te + O
A_u (IR)	**121.553**	**Sr** + Te + O	**B_u (IR)**	**143.457**	**Sr** + Te + O
A_u (IR)	**129.906**	**Sr** + Te + O	**B_u (IR)**	**210.839**	Te + **O**
A_u (IR)	**195.866**	Te + **O**	**B_u (IR)**	**218.301**	**O**
A_u (IR)	**209.873**	Sr + Te + **O**	**B_u (IR)**	**238.850**	**O**
A_u (IR)	**231.784**	Sr + Te + **O**	**B_u (IR)**	**315.355**	Te + **O**
A_u (IR)	**316.640**	Te + **O**	**B_u (IR)**	**340.004**	**O**
A_u (IR)	**347.006**	**O**	**B_u (IR)**	**384.224**	**O**
A_u (IR)	**381.705**	**O**	**B_u (IR)**	**434.590**	**O**
A_u (IR)	**434.871**	**O**	**B_u (IR)**	**485.785**	**O**
A_u (IR)	**507.483**	Te + **O**	**B_u (IR)**	**513.346**	**O**
A_u (IR)	**514.950**	**O**	**B_u (IR)**	**536.596**	**O**
A_u (IR)	**563.441**	**O**	**B_u (IR)**	**578.382**	**O**
A_u (IR)	**592.740**	Te + **O**	**B_u (IR)**	**642.991**	**O**
A_u (IR)	**671.006**	**O**			

LP and HP1 phases. Low-frequency modes (<150 cm^{-1}) have significant contributions from all three atoms (Sr, Te, O), indicating collective lattice dynamics. In the mid-frequency range (150–400 cm^{-1}), Te–O hybridization dominates, with strong coupling between Te and O atoms. High-frequency modes (>650 cm^{-1}) are mainly oxygen-dominated; however, they also show a considerable contribution from tellurium. This indicates that the Te–O covalent bonding in the HP3 phase is stronger under pressure than in the LP and HP1 phases.

The HP4 phase of $SrTeO_4$, like HP3, crystallizes in a monoclinic structure that can also be described by the space group $P2_1/c$ ($P2_1/c$ and $P2_1/n$ are two different notations for the same monocyclic space group). The crystal structure of phase HP4 belongs to the C_{2h} point group. Since HP4 shares symmetry and number of atoms per unit cell with HP3, the same number of modes with the same symmetry are expected. However, the distribution of phonon modes and atomic contributions show significant differences between the two phases due to pressure-induced structural changes at 80 GPa. In comparison with the LP and HP1 phases (both orthorhombic, D_{2h} symmetry), the number of Raman- and IR-active modes in HP4 increases, indicating reduced symmetry and increased complexity of the structure under high pressure. The eigenvector analysis indicates that in the low-frequency range (<150 cm^{-1}), vibrations are mainly related to Sr atoms, consistent with observations in other phases. However, in contrast to LP and HP1, the contributions of Te atoms in the mid- and high-frequency regions are greater in HP4, indicating stronger Te–O bonding under high pressure. In addition, high-frequency Raman-active and IR-active modes (extending up to 668 cm^{-1}) are still largely dominated by O atoms; nevertheless, considerable Te–O hybridization is also seen, especially in the modes between 550–600 cm^{-1}. This confirms previous observations that Te–O covalent bonding remains strong and could be significantly increased in HP4. The HP4 phase shows slightly lower phonon frequencies for the high-frequency modes com-

pared to HP3, a detail that will be further discussed in the following analysis.

The phonon dispersion curves and the corresponding and the total and partial phonon density of states (PDOS) for $SrTeO_4$ in the LP (0 GPa), HP1 (0 GPa), HP3 (7 GPa), and HP4 (80 GPa) phases are shown in Fig. 6. All four phases contain positive phonon frequencies throughout the Brillouin zone, suggesting that they are dynamically stable at the corres-

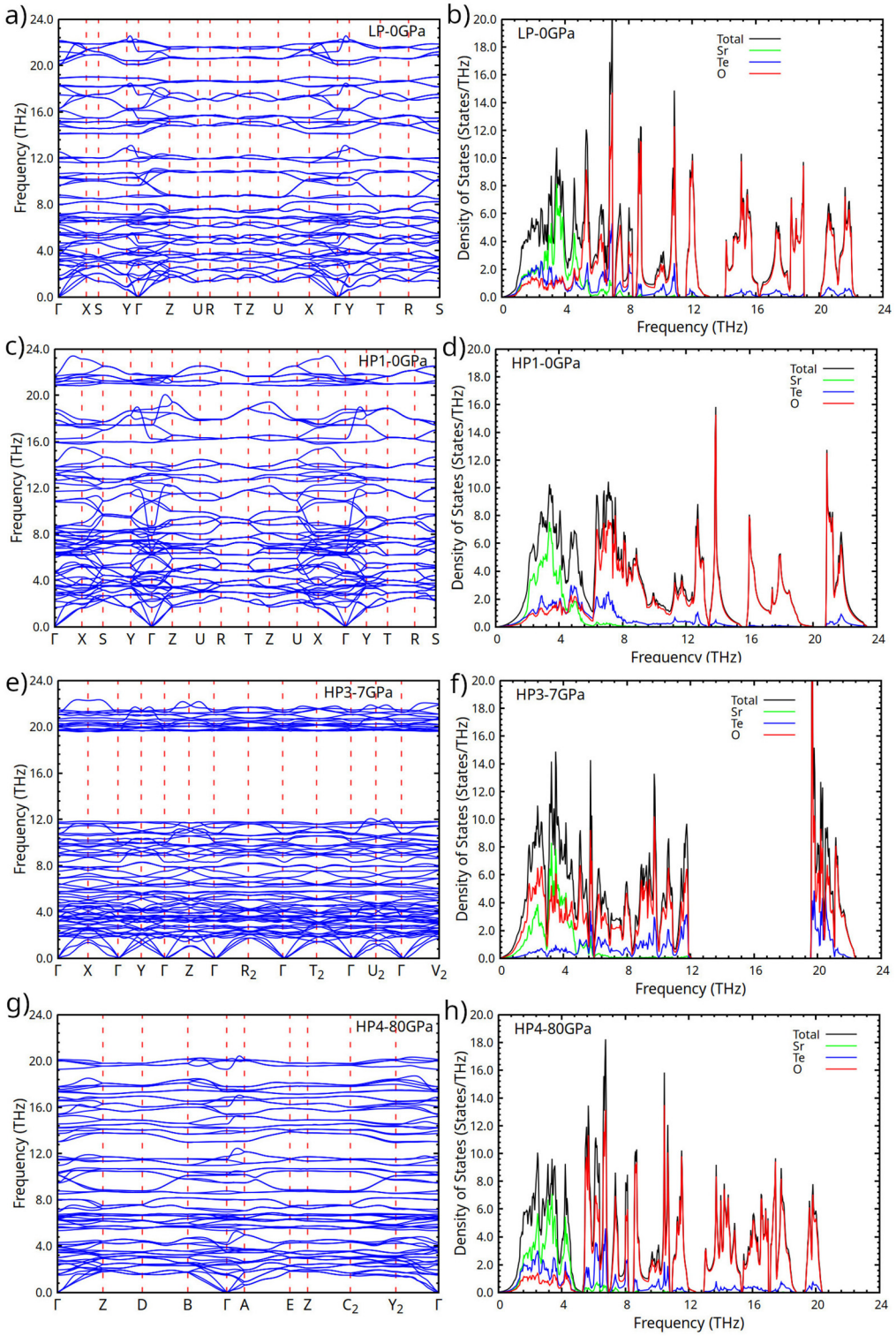

Fig. 6 The phonon dispersion curves (left panels) and the corresponding total and partial phonon density of states (PDOS) (right panels) for $SrTeO_4$ at various phases and pressures: (a, b) the LP phase at 0 GPa, (c, d) the HP1 phase at 0 GPa, (e, f) the HP3 phase at 7 GPa, and (g, h) the HP4 phase at 80 GPa.

ponding pressures. The phonon dispersion curves of the LP phase of $SrTeO_4$ are divided into three distinct regions: a low-frequency region (LFR) extending from 0 to 13 THz, an intermediate-frequency region (IFR) ranging from 14 to 19 THz, and a high-frequency region (HFR) above 19 THz. The LFR consists of three acoustic branches and forty-four optical phonon branches, which exhibit a relatively high dispersion. The LFR and the IFR are separated by a phonon gap of approximately 1.0 THz, which is probably the result of the mass difference between the different types of atoms in the unit cell. The IFR and HFR include 16 and 9 optical phonon modes, respectively, and are separated by a phonon gap of about 1 THz. The first region, below 5.5 THz, is dominated by vibrations of Sr atoms, with significant contributions from strong Te–O hybridization. The result agrees with our previous electronic structure analysis and further supports strong Te–O bonding. In the frequency range between 5.5 and 13 THz, the phonon modes are dominated by oxygen atoms. Although Te–O hybridization is still present in this region, it is weaker than that in the lower-frequency modes. The contribution of Sr atoms to the phonon modes disappears above approximately 8 THz. As expected, the intermediate- and high-frequency regions are dominated by oxygen vibrations, the lightest element of $SrTeO_4$. The contribution of Te atoms in this frequency range is quite small. The appearance of high-frequency Te-related modes, despite Te being heavier than Sr, provides additional evidence of stronger Te–O bonds.

The phonon dispersion curves of the HP1 phase are broadly similar in both shape and frequency range to those of the LP phase. In the LP phase, four optical phonon modes about 12 THz are separated from lower-frequency modes in the LFR by a phonon gap of about 0.1 THz. In the HP1 phase, the small gap closes and the LFR increases to 15.8 THz, about 4 THz higher than the LP phase. In the HP1 phase, the LFR is separated from the IFR by a gap of only 0.1 THz, while the corresponding gap in the LP phase is approximately 1 THz. The highest phonon frequency increases from 22.4 THz in the LP phase to 23.2 THz in the HP1 phase. Similar to the LP phase, Sr atoms dominate the low-frequency region of the HP1 phase, with vibrational contributions extending up to about 8 THz. Strong Te–O hybridization is observed in the HP1 phase below 5.5 THz, which is also comparable to the LP phase. This implies that the atoms in both structures have the ability to create strong covalent bonds. The IFR and HFR regions are mainly characterized by oxygen vibrations in the HP1 phase, similar to the LP phase. Te atoms continue to make minor contributions to the HFR region, despite their heavier mass. This indicates that the Te–O bonds are also stronger than the Sr–O bonds in this phase.

The phonon dispersion curves of the HP3 phase at 7 GPa is substantially different from those of the LP and HP1 phases. The LP and HP1 phases have three separate regions divided by minor gaps, whereas the HP3 phase spectrum is clearly divided into only two main parts, separated by a significantly larger phonon gap of about 8 THz. Sr atoms again dominate the low-frequency region, with their vibrational contributions extending up to approximately 7.2 THz. In the frequency range below 5.5 THz, the vibrational contribution of O atoms is greater in HP3 than in the LP and HP1 phases. Also, Te atoms show increased vibrational activity in the HFR region compared to the LP and HP1 phases. The increased vibrational activity of the heavier Te atoms in the HFR region implies that the Te–O covalent bonds are stronger in the HP3 phase.

The phonon curve of the HP4 phase at 80 GPa significantly differs from that of HP3; however, it has a general similarity to the phonon curve of the LP and HP1 phases. As in the LP and HP1 phases, the phonon spectrum of HP4 is also divided into three regions: LFR, IFR, and HFR. However, unlike LP and HP1, where the phonon gaps between LFR–IFR and IFR–HFR are about 1 THz, in HP4 these gaps are significantly reduced to approximately 0.2 THz. The decrease in phonon gaps can be related to the higher pressure (80 GPa), which increases interatomic interactions and reduces the vibrational difference between different types of atoms. Similarly to the LP and HP1 phases, Sr atoms in the HP4 phase mainly contribute to the low-frequency region, with vibrations extending up to approximately 7.8 THz. In the same region, significant Te–O hybridization is observed, signifying the existence of strong covalent interaction between Te and O atoms. In the IFR and HFR regions, oxygen vibrations remain dominant; however, the vibrational contribution of Te atoms in these regions is noticeably higher compared to the LP and HP1 phases. This increase suggests that the Te–O covalent bonding in HP4 is stronger than in the lower-pressure phases. Finally, the maximum phonon frequency in the HP4 phase is found to be lower than that of the other phases. This decrease may indicate that, under high pressure, structural changes result in a decrease in the average bond stiffness of the system. In particular, increased directionality in Te–O bonding and the formation of new coordination environments may suppress certain high-frequency vibrational modes, thereby reducing the upper limit of the phonon spectrum. The results clearly show the impact of pressure on the vibrational properties and bonding characteristics of $SrTeO_4$ in its various phases.

Recently there have been found many compounds formed by chalcogen elements which undergo metallization under compression.[40] In these compounds usually the transition to the metallic state has been considered as a precursor to superconductivity.[40] Given the predicted metallization of $SrTeO_4$ we have explored if this compound could become a superconductor under HP. Taking advantage of phonon calculations, we also employed linear response theory together with the Migdal–Eliashberg formalism to investigate the electron–phonon interaction and the possibility of conventional phonon-mediated superconductivity in $SrTeO_4$ up to 100 GPa. Although the pressure-induced metallization is observed in $SrTeO_4$, there is no evidence of superconductivity at pressures up to 100 GPa. The calculated electron–phonon coupling parameters (λ) are 0.00345 at 80 GPa and 0.01020 at 100 GPa. These values of the electron–phonon coupling are too small, leading to weak lattice distortions and hindering superconducting pairing correlations. Using the electron–phonon coup-

Table 8 Summary of the main results reported in this work for the different phases of $SrTeO_4$ including the coordination number of Sr and Te. The band-gap energy (E_g) is given at the transition pressure. More information can be found in the previously reported tables

Phase	Pressure range (GPa)	Space group	K_0 range	E_g (eV)	CN Sr	CN Te
LP	0–2.5	***Pbcn***	73	2.04	6	6
HP1	2.5–7	***Pbcm***	103	1.02	9	6
HP3	7–80	$P2_1/c$	153	0.73	10	5
HP4	80–100	$P2_1/n$	175	0	11	7

ling parameter (λ), the logarithmic average phonon frequency (ω_{ln}) is calculated to be 538.3 K at 80 GPa and 505.8 K at 100 GPa. The extremely weak electron–phonon coupling suggests that lattice vibrations have minimal influence on Cooper pair formation and therefore likely suppress the emergence of superconductivity, even after metallization. In addition, the calculated superconducting critical temperatures (T_c) are as low as 0.001 K at 80 GPa and 0.002 K at 100 GPa, indicating a negligible possibility of superconductivity in the high-pressure metallic phase.

4. Conclusions

In this study, we examined the behavior of $SrTeO_4$ under high pressures up to 100 GPa by applying the density-functional theory. Our findings indicate that the GGA-PBE approximation effectively characterizes the crystal structure at ambient pressure. Additionally, we characterized the high-pressure behavior of $SrTeO_4$ up to 100 GPa. Table 8 summarizes the stability of different phases of $SrTeO_4$ and their properties. We discovered that $SrTeO_4$ is anticipated to experience three phase transitions at pressures of 2.5, 7, and 80 GPa, respectively. The crystal structures corresponding to these three high-pressure phases are documented. These transitions result in successive reductions of the unit-cell volume and alterations in the coordination polyhedra of Sr and Te. Such structural modifications influence the electronic and vibrational properties of the compound under investigation, which have been systematically analyzed in our research. Notably, we observed that pressure induces a pressure-driven metallization of $SrTeO_4$, which is associated with the changes in Te–O bonding caused by the increased hybridization between Te 5d and O 2p orbitals. Furthermore, we explored the possibility of inducing superconductivity in $SrTeO_4$ through pressure using the Migdal–Eliashberg formalism and concluded that the material is not expected to exhibit superconductivity up to 100 GPa. Our results offer essential insights into the crystal symmetry, electronic characteristics, and lattice dynamics of $SrTeO_4$. The insights gained from this work are vital for improving our understanding of the behavior of tellurates under compression. We anticipate that the results presented in this study will stimulate experimental investigations that provide structural, electronic, and vibrational data for comparison and interpretation in future experiments. Powder X-ray diffraction, Raman, and resistivity experiments performed using diamond-anvil cells would be requested to confirm the predicted phase transitions and metallization.

Author contributions

E. Karaca: investigation, software, formal analysis, data curation, and writing – review and editing. D. Errandonea: conceptualization, methodology, validation, resources, supervision, funding acquisition, and writing – review and editing.

Conflicts of interest

The authors declare that they have no known competing financial interests or personal relationships that could have appeared to influence the work reported in this paper.

Data availability

Data will be made available by the authors upon reasonable request.

The SI contains the convergence tests performed to decide the energy cut-off and K-point mesh used in calculations. See DOI: **https://doi.org/10.1039/d5dt01643f**.

Acknowledgements

Calculations were performed on the Viking cluster at the High Performance Computing Facility of the University of York. The authors acknowledge the computational support of the University of York HPC Service. D. E. acknowledges the support from Generalitat Valenciana under grants CIPROM/2021/075 and MFA/2022/007 and Spanish Ministerio de Ciencia, Innovación y Universidades and Agencia Estatal de Investigación (MCIN/AEI/10.13039/501100011033) and the European Union under grant PID2022-138076NB-C41. This study is part of the Advanced Materials Program supported by MCIU with funding from NextGenerationEU (PRTR-C17.I1) and Generalitat Valenciana.

References

1 D. Hamani, A. Mirgorodsky, O. Masson, T. Merle-Méjean, M. Colas, M. Smirnov and P. Thomas, *J. Solid State Chem.*, 2011, **184**, 637–643.
2 D. Hamani, A. Plat, M. Colas, J. Cornette, O. Masson, A. Mirgorodsky and P. Thomas, *J. Alloys Compd.*, 2016, **661**, 92–99.

3 J. Qu, L. Yan, H. Liu, Q. Tao, P. Zhu, Z. Li and X. Wang, *High Press. Res.*, 2021, **41**, 318–327.
4 L. Liu, H. Skogby, S. Ivanov, M. Weil, R. Mathieu and P. Lazor, *Chem. Commun.*, 2019, **55**, 12000–12003.
5 S. Sondarva and D. Shah, *Mater. Today Proc.*, 2021, **47**, 711–714.
6 Y. Chen, X. Li, K. Liu, Q. Su, H. Wang, R. Mathieu, S. Ivanov, M. Weil, H. Y. Geng, Z. Zhang, *et al.*, *J. Phys. Chem. Lett.*, 2025, **16**, 3509–3517.
7 P. Pramanik, F. Eder, M. Weil, S. Ivanov, P. Maltoni, R. Miletich, T. Edvinsson and R. Mathieu, *Phys. Rev. B*, 2024, **110**, 054104.
8 W.-H. Li, C.-W. Wang, D. Hsu, C.-H. Lee, C.-M. Wu, C.-C. Chou, H.-D. Yang, Y. Zhao, S. Chang, J. W. Lynn, *et al.*, *Phys. Rev. B: Condens. Matter Mater. Phys.*, 2012, **85**, 094431.
9 S. Podchezertsev, N. Barrier, A. Pautrat, E. Suard, M. Retuerto, J. A. Alonso, M. T. Fernández-Díaz and J. Rodríguez-Carvajal, *Inorg. Chem.*, 2021, **60**, 13990–14001.
10 M. Abubakr, K. Fatima, Z. Abbas, A. Hussain, N. Jabeen, H. H. Raza, Y. Chaib, S. Muhammad, S. M. Siddeeg and I. Gorczyca, *J. Solid State Chem.*, 2022, **305**, 122689.
11 M. G. Kanatzidis, *Chem. Mater.*, 2010, **22**, 648–659.
12 G. Liu, C. Yan, Z. Xue, C. Liu, G. Xu and T. Wang, *Nanosclae*, 2018, **10**, 12284–12290.
13 J. S. Schilling, *J. Phys. Chem. Solids*, 1998, **59**, 553–568.
14 D. Errandonea and F. J. Manjón, *Prog. Mater. Sci.*, 2008, **53**, 711–773.
15 D. Errandonea and A. B. Garg, *Prog. Mater. Sci.*, 2018, **97**, 123–169.
16 W. Crichton, M. Merlini, H. Müller, J. Chantel and M. Hanfland, *Mineral. Mag.*, 2012, **76**, 913–923.
17 E. Bandiello, D. Errandonea, D. Martinez-Garcia, D. Santamaria-Perez and F. Manjón, *Phys. Rev. B: Condens. Matter Mater. Phys.*, 2012, **85**, 024108.
18 D. Errandonea, A. Muñoz, P. Rodríguez-Hernández, O. Gomis, S. N. Achary, C. Popescu, S. J. Patwe and A. K. Tyagi, *Inorg. Chem.*, 2016, **55**, 4958–4969.
19 J. W. Otto, J. K. Vassiliou, R. F. Porter and A. L. Ruoff, *Phys. Rev. B: Condens. Matter Mater. Phys.*, 1991, **44**, 9223.
20 D. Errandonea, R. Kumar, J. Lopez-Solano, P. Rodríguez-Hernández, A. Muñoz, M. Rabie and R. Sáez Puche, *Phys. Rev. B: Condens. Matter Mater. Phys.*, 2011, **83**, 134109.
21 M. Hladik, A. Penz, F. R. Purtscher, T. S. Hofer, G. Heymann and M. Weil, *Dalton Trans.*, 2024, **53**, 19214–19225.
22 M. Ibarra Castro, J. Almanza Robles, D. Cortés Hernandez, J. Escobedo Bocardo and J. Torres Torres, *Ceram. Int.*, 2010, **36**, 1205–1210.
23 D. Hottentot and B. Loopstra, *Struct. Sci.*, 1979, **35**, 728–729.
24 J. Lapasset and J. Moret, *Cryst. Struct. Commun.*, 1985, **41**, 1558–1562.
25 A. Benmakhlouf, D. Errandonea, M. Bouchenafa, S. Maabed, A. Bouhemadou and A. Bentabet, *Dalton Trans.*, 2017, **46**, 5058–5068.
26 J. P. Perdew, K. Burke and M. Ernzerhof, *Phys. Rev. Lett.*, 1996, **77**, 3865.
27 P. Giannozzi, S. Baroni, N. Bonini, M. Calandra, R. Car, C. Cavazzoni, D. Ceresoli, G. L. Chiarotti, M. Cococcioni, I. Dabo, *et al.*, *J. Phys.: Condens. Matter*, 2009, **21**, 395502.
28 P. Giannozzi, O. Andreussi, T. Brumme, O. Bunau, M. B. Nardelli, M. Calandra, R. Car, C. Cavazzoni, D. Ceresoli, M. Cococcioni, *et al.*, *J. Phys.: Condens. Matter*, 2017, **29**, 465901.
29 A. M. Rappe, K. M. Rabe, E. Kaxiras and J. Joannopoulos, *Phys. Rev. B: Condens. Matter Mater. Phys.*, 1990, **41**, 1227.
30 C. Chen, R. Appleton, S. Mishra, K. Nykiel and A. Strachan, *npj Comput. Mater.*, 2025, **11**, 191.
31 T. Ouahrani, R. M. Boufatah, M. Benaissa, A. Morales-García, M. Badawi and D. Errandonea, *Phys. Rev. Mater.*, 2023, **7**, 025403.
32 H. J. Monkhorst and J. D. Pack, *Phys. Rev.*, 1976, **13**, 5188.
33 S. Baroni, P. Giannozzi and E. Isaev, *Rev. Mineral. Geochem.*, 2010, **71**, 39–57.
34 A. Migdal, *Sov. Phys. JETP*, 1958, **7**, 996–1001.
35 G. Eliashberg, *Sov. Phys. JETP*, 1960, **11**, 696–702.
36 P. B. Allen and R. Dynes, *Phys. Rev. B*, 1975, **12**, 905.
37 P. Allen and R. Dynes, *J. Phys. C: Solid State Phys.*, 1975, **8**, L158.
38 E. Karaca and D. Errandonea, *Results Phys.*, 2023, **50**, 106581.
39 E. Karaca and D. Errandonea, *Results Phys.*, 2024, **57**, 107330.
40 W. Zhong, H. Zhang, E. Karaca, J. Zhou, S. Kawaguchi, H. Kadobayashi, X. Yu, D. Errandonea, B. Yue and F. Hong, *Phys. Rev. Lett.*, 2024, **133**, 066001.
41 J. P. Bastide, *J. Solid State Chem.*, 1987, **71**, 116.
42 S. López-Moreno and D. Errandonea, *Phys. Rev. B: Condens. Matter Mater. Phys.*, 2012, **86**, 104112.
43 T. Ouahrani, A. Muñoz, R. Franco, R. Boufatah, Z. Bedrane and D. Errandonea, *J. Alloys Compd.*, 2024, **978**, 173483.
44 G. Murphy, B. J. Kennedy, B. Johannessen, J. A. Kimpton, M. Avdeev, C. S. Griffith, G. J. Thorogood and Z. Zhang, *J. Solid State Chem.*, 2016, **237**, 86–92.
45 T. Huang, J.-S. Lee, J. Kung and C.-M. Lin, *Solid State Commun.*, 2010, **150**, 1845–1850.
46 M. Weil, B. Stöger, C. Gierl-Mayer and E. Libowitzky, *J. Solid State Chem.*, 2016, **241**, 187–197.
47 D. Errandonea and F. J. Manjón, *Prog. Mater. Sci.*, 2008, **53**, 711–773.
48 F. Birch, *Phys. Rev.*, 1947, **71**, 809–824.
49 D. Errandonea, A. Muñoz, P. Rodríguez-Hernández, J. E. Proctor, F. Sapiña and M. Bettinelli, *Inorg. Chem.*, 2015, **54**, 7524–7535.
50 A. Girard, M. Stekiel, D. Spahr, W. Morgenroth, B. Wehinger, V. Milman, T. Nguyen-Thanh, A. Mirone, A. Minelli, L. Paolasini, A. Bosak and B. Winkler, *J. Phys.: Condens. Matter*, 2018, **31**, 055703.
51 J. Gleissner, D. Errandonea, A. Segura, J. Pellicer-Porres, M. A. Hakeem, J. E. Proctor, S. V. Raju, R. S. Kumar,

P. Rodríguez-Hernández, A. Muñoz, S. Lopez-Moreno and M. Bettinelli, *Phys. Rev. B*, 2016, **94**, 134108.

52 G. L. Murphy, Z. Zhang, H. E. Maynard-Casely, J. Stackhouse, P. M. Kowalski, T. Vogt, E. V. Alekseev and B. J. Kennedy, *Acta Mater.*, 2023, **243**, 118508.

53 D. Errandonea, J. Pellicer-Porres, F. J. Manjón, A. Segura, C. Ferrer-Roca, R. S. Kumar, O. Tschauner, P. Rodríguez-Hernández, J. López-Solano, S. Radescu, A. Mujica, A. Muñoz and G. Aquilanti, *Phys. Rev. B: Condens. Matter Mater. Phys.*, 2005, **72**, 174106.

54 D. Errandonea, R. S. Kumar, X. Ma and C. Tu, *J. Solid State Chem.*, 2008, **181**, 355–364.

55 R. M. Hazen and C. T. Prewitt, *Am. Mineral.*, 1977, **62**, 309–315.

56 T. Garcia-Sanchez, D. Diaz-Anichtchenko, A. Muñoz, P. Rodriguez-Hernandez, T. Marqueño, M. Jafar, S. N. Achary, F. Alabarse and D. Errandonea, *J. Phys. Chem. C*, 2023, **127**, 2069–2077.

57 M. Weil, P. Pramanik, P. Maltoni, R. Clulow, A. Rydh, M. Wildner, P. Blaha, G. King, S. A. Ivanov, R. Mathieu and H. Singh, *Mater. Adv.*, 2024, **5**, 3001–3013.

58 V. Monteseguro, J. Ruiz-Fuertes, J. Contreras-García, P. Rodríguez-Hernández, A. Muñoz and D. Errandonea, *Appl. Phys. Lett.*, 2019, **115**, 012102.